International Journal of Heat and Mass Transfer 171 (2021) 121085

Contents lists available at ScienceDirect

International Journal of Heat and Mass Transfer

journal homepage: www.elsevier.com/locate/hmt

Microscale Knudsen Effect over the Transverse Thermal Conductivity of Woven Ceramic Fabrics Under Compression

Rodrigo Penide-Fernandez [a], Frederic Sansoz [a,b,*]

[a] Department of Mechanical Engineering, The University of Vermont, Burlington, VT 05405, USA
[b] Material Science program, The University of Vermont, Burlington, VT 05405, USA

ARTICLE INFO

Article history:
Received 17 October 2020
Revised 17 December 2020
Accepted 6 February 2021

Keywords:
Hi-Nicalon
Nextel
Thermal conductivity
Microscale Knudsen effect
Finite element analysis
Multiscale modeling

ABSTRACT

Woven-fiber ceramic materials have shown remarkable results in the design of insulative lay-up structures for flexible thermal protection systems. A deeper understanding of heat transfer through the different insulation layers is key for predicting the performance of heat shields. In this article, a thermo-mechanical multiscale model is developed to predict the out-of-plane thermal conductivity at the micro- and meso-levels of transversely loaded two-dimensional woven ceramic fabrics. Knudsen effects within the multiscale structure are studied by adjusting gas pressure conditions. Alumina-based Nextel-BF20 and silicon carbide Hi-Nicalon with a 5-harness satin weave pattern are modeled by finite-element analysis. The computational results are validated experimentally by applying the anisotropic transient plane source method. We find that out-of-plane thermal conductivity decreases significantly with gas pressure due to Knudsen effects in the confined air within the fibrous structure. The dependence of thermal conductivity of fabrics on fiber volume fraction is shown to decrease markedly with pressure reduction. The proposed multiscale modeling approach yields a notable accuracy improvement, with respect to simplified series-parallel models, when compared with our experimental measurements. The FEA model is applicable to other fabric materials and loading conditions and presents an opportunity to study how changes at the fiber level affect the overall thermal behavior of woven fabrics.

1. Introduction

Current Entry, Decent and Landing (EDL) systems are expected to face important challenges with the increasing landed payload weight and size in future space missions. Deployable aeroshells like the Hypersonic Inflatable Aerodynamic Decelerator (HIAD) have been proposed to overcome such challenges. The larger drag area attainable with this system can significantly reduce ballistic coefficients and afford higher Mach numbers and dynamic pressures. Despite the lower entry heating produced by a lower ballistic coefficient, hypersonic atmospheric entry still produces considerable aerothermal loads for the aeroshell to require a flexible Thermal Protection System (TPS) [1].

The precise modeling of the out-of-plane thermal conductivity of the outer woven ceramic fabric is crucial for the design and analysis of the lay-up structure that integrates the HIAD's flexible TPS [1]. Here, a fabric is viewed as a multiscale composite with a porous structure consisting of a woven-fiber material and a gaseous matrix organized in 3 distinctive levels: Fabric, yarn and fiber as shown in Fig. 1. At microscopic scale, the properties of the fibers and confined gas together with their arrangement in the yarn control the thermal behavior of the yarn. Analogously, the arrangement and effective thermal properties of the yarns and gas determine the fabric properties at the mesoscale. In our previous work [2], a finite-element analysis (FEA) methodology to quantify the anisotropic thermal conductivity of two-dimensional woven ceramic fiber materials was proposed and validated using hot-disk transient plane experiments. The model provided useful insights into heat conduction at the mesoscale in fabric materials under a transversal compressive load. A parametric study showed that to capture the correct behavior of the fabric in the out-of-plane direction, a better description of the thermal behavior of confined air was necessary [2].

Kaganer [3] described how the thermal conductivity of a gas is affected by being confined within a space with a characteristic length close or smaller to that of its molecular mean free path. Several researchers have used this description to model gas conduction in porous materials, such as spherical beds or aerogels [4-7]. Others [8,9] have used one-dimensional differential equation formulations to describe the thermal conductivity and transient behavior of lay-ups of fibrous insulators while accounting

* Corresponding author.
E-mail address: frederic.sansoz@uvm.edu (F. Sansoz).

https://doi.org/10.1016/j.ijheatmasstransfer.2021.121085
0017-9310/

Nomenclature

440	Nextel fiber type
5HS	5-harness satin weave type
BF20	Nextel fabric type
DEM	discrete element method
FEA	finite element analysis
HIAD	hypersonic inflatable aerodynamic decelerator
RVE	representative volume element
SEM	scanning electron microscopy
TPS	transient plane source
A	cross-sectional area of the RVE
Cond	gap thermal conductance
C_p	specific heat capacity at constant pressure
C_v	specific heat capacity at constant volume
D	dimensionless function
D_f	diameter of the fiber
d_1	characteristic length of a pore in the vertex region
d_2	characteristic length of a gap within fibers in the edge region
d_g	diameter of the gas molecule
E	Young's modulus
K_{air}	thermal conductivity of air
K_{air0}	thermal conductivity of air in STP conditions
K_{fiber}	thermal conductivity of a fiber
k_B	Boltzmann's constant
K_{eff}	effective thermal conductivity of the model
Kn	Knudsen number
K_{in}	effective thermal conductivity in the in-plane
K_{out}	effective thermal conductivity in the out-of-plane
L	dimension of the microscale model
L_C	characteristic length
P	gas pressure
P_0	output power
Pr	Prandtl number
Q	Heat flow
r	radius of the sensor
T	temperature
V_{fiber}	volume fraction of fiber
V^0_{fiber}	initial volume fraction of fiber
x	distance travelled by the heat

Greek letters

α	accommodation coefficient
γ	adiabatic coefficient
Δ	difference operator
ϵ	strain
κ	thermal diffusivity
λ	molecular mean free path
ρ	density
σ	stress
τ	dimensionless time

Subscripts

0	initial condition
air	air property
eff	effective property
f	fiber property
g	gas property
in	in-plane property
out	out-of-plane property
p	constant pressure
v	constant volume

Superscripts

0	initial property

for confined gas effects. Daryabeigi et al. [10,11] studied the effect of pressure and temperature on the heat transfer of non-woven insulators for thermal protection systems, the gas behavior was modeled as a standard gas conduction model, using Kaganer's correction with an empirical fit for the characteristic length of the pore. Zhao et al. [12] applied the same methodology to treat the gas behavior in different fibrous materials. Lurie et al. [13] studied the influence of mean distance between fibers in the effective gas conductivity for non-woven materials. Despite all efforts, it is a general practice to treat thermal conductivity through fibrous insulators as a mixed series-parallel model or to use a semi-empirical formulation or an analytical solution of a simplified problem. However, a thermo-mechanical physics-based multiscale model that accurately captures the gas behavior at both micro- and meso-levels is still lacking to simulate the effective out-of-plane behavior of heat conduction through woven insulators.

The objective of this article is to develop a new thermo-mechanical FEA model for the out-of-plane thermal conductivity across the multiscale 3D structure of woven fabrics to more accurately simulate and understand the effects of mechanical strain and gas pressure. The FEA results are then compared to hot-disk transient plane source experiments conducted under variable pressure. This article is organized as follows. Section 2 describes the experimental methodology and woven ceramic materials tested in this study. Section 3 presents the proposed model for the intra-yarn heat-transfer at microscale that takes air pressure into account. Section 4 focuses on the dynamical behavior and heat-transfer simulations in the woven fabrics at the meso-level, where results from both FEA models and hot-disk measurements are compared. The effects of gas pressure and micro-spacing in woven fabric materials, as well as, a comparison between the two studied materials, and advantages and limitations of the proposed multiscale model, are discussed in Section 5.

2. Materials and experimental methods

2.1. Materials

Alumina-based Nextel-BF20 (3M, St Paul, MN, USA) and silicon carbide Hi-Nicalon (COI ceramics Inc., San Diego, CA, USA) woven fabrics with a 5-harness satin pattern were used for this study. The fabrics were cut in 40 × 40 mm^2 samples using a rotary blade and a self-healing mat to minimize distortion.

The fiber of Nextel-BF20 fabrics, Nextel-440, is an aluminoborosilicate material with a composition of Al_2O_3 70 wt%, SiO_2 28 wt%, B_2O_3 2 wt% [14]. The fibers had a filament diameter of 10–12 µm and the nominal filament count for a single yarn was 750 fibers. Prior to testing, the organic sizing of the Nextel fabric was removed by heat cleaning following the protocol suggested by the manufacturer. The samples were place into a furnace at room temperature, the temperature was ramped up to 700°C in 45 minutes and then kept at the prescribed temperature for 1 hour. The samples were left to cool to room temperature inside the oven [15]. Due to the lack of literature data on the thermal conductivity of Nextel 440 fibers, it was approximated to that of mullite, 7 W/m/K [16]. The density was equal to 3.05 ± 0.03 g/cm^3, measured with a pycnometer and a high-precision scale.

Hi-Nicalon fibers consisted of a β-SiC nanocrystalline structure with a composition of Si 62 wt%, C 37 wt% and O 0.5 wt% [17]. The fibers had a filament diameter of 14 µm and a nominal filament count of 500 fibers per yarn. A thermal conductivity of 8 W/m/K [18] was used for the Hi-Nicalon fibers. A density of 2.68 ± 0.03 g/cm3 was found by applying the above methodology.

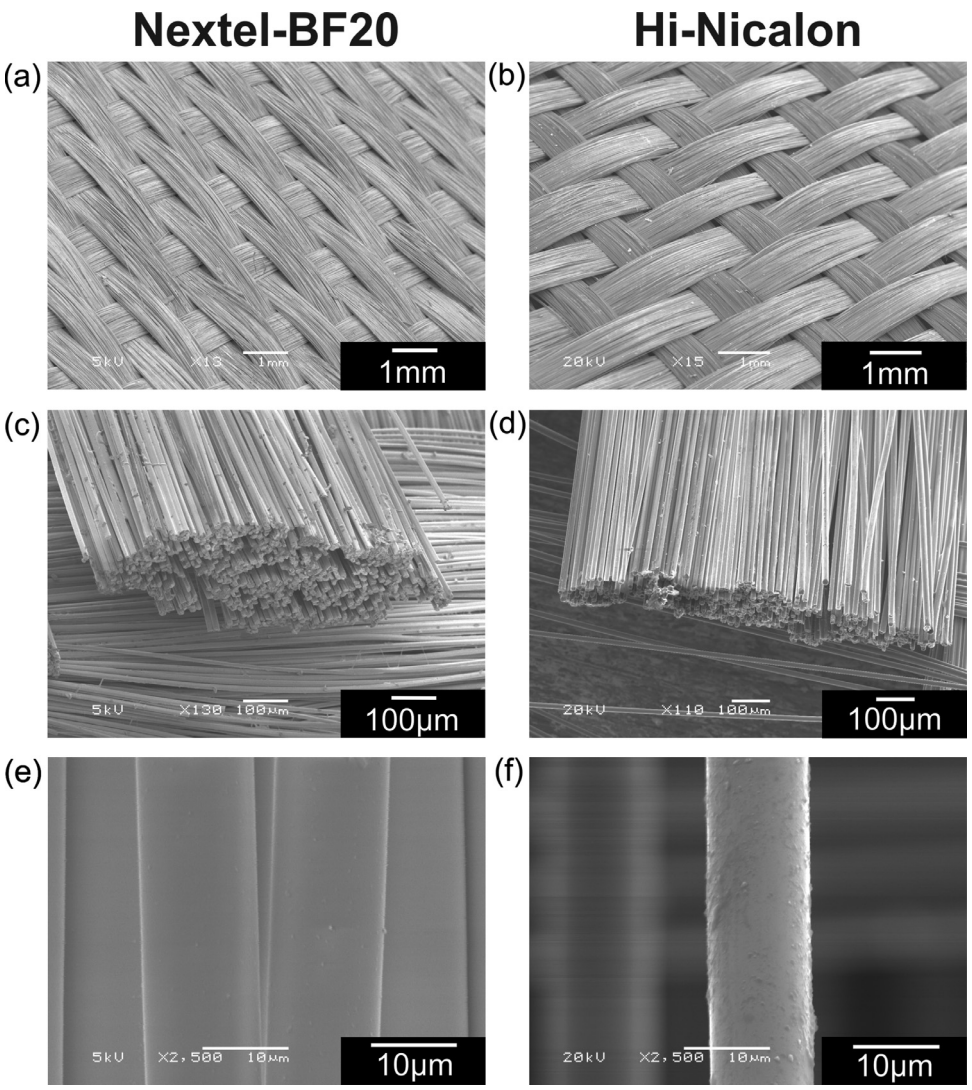

Fig. 1. Alumina-based Nextel-BF20 and SiC Hi-Nicalon woven fabrics. Scanning electron microscopy images of (a)-(b) Meso-scale view of as-received woven fabrics, (c)-(d) Micro-scale yarn sections, and (e)-(f) single fibers for heat-cleaned Nextel-440 and Hi-Nicalon, respectively.

2.2. Experimental procedure

Thermal conductivity was measured by the hot-disk transient plane source method. This technique is based on the use of a plane element that acts both as temperature sensor and heat source [19-22]; the sensor was placed between two plies of 4 fabric samples as illustrated in Fig. 2. This technique measures in-plane and out-of-plane thermal conductivity and diffusivity simultaneously. The hot-disk transient plane source method is further discussed in detail elsewhere [2]. A TPS2200 analyzer (Thermtest, Fredericton, NB, Canada), which had an accuracy >95% and repeatability >99% was used for data acquisition and postprocessing.

Under the assumption of transversely isotropic infinite media, and by spatially averaging the temperature over the area of the sensor, the solution of Fourier's law for heat conduction applied to this system is [19-22]:

$$\Delta\bar{T}(\tau_{in}) = \left(\frac{P_0}{\left(\pi^{\frac{3}{2}} r\sqrt{K_{in}K_{out}}\right)}\right) D(\tau_{in}) \tag{1}$$

where $\tau_{in} = \sqrt{\kappa_{in}t}/r$ is a dimensionless time parameter.

By iteration over the thermal diffusivity $\kappa_{in} = K_{in}/(\rho C_p)$, τ_{in} was computed to yield a linear relation between $\Delta\bar{T}(\tau_{in})$ and $D(\tau_{in})$. From the slope of Eq. (1), the anisotropic experiment yields the product $K_{in}K_{out}$. Finally, the volumetric heat capacity (ρC_p) was used to de-couple the conductivity values.

The volumetric heat capacity (ρC_p) was measured using the heat capacity module of the TPS2200 analyzer. However, the heat capacity measured using this method corresponds to that of a solid material without pores. Values of 2.3317 ± 0.0031 MJ/m^3/K and 1.8126 ± 0.0028 MJ/m^3/K were found for Nextel-440 and Hi-Nicalon, respectively. Similar values have been reported for fibers with a composition and structure close to those of Hi-Nicalon [23]. By describing the fabric to be a composite with a gaseous matrix, however, a rule of mixtures was applied to account for the air contribution, such as

$$(\rho C_p)_{fabric} = V_{fiber}(\rho C_p)_{fiber} + \left(1 - V_{fiber}\right)(\rho C_p)_{air} \tag{2}$$

where V_{fiber} is the volume fraction of ceramic fibers.

Compressive strain was incrementally applied to the fabric samples (Fig. 2) to study the effect of deformation on the out-of-plane thermal conductivity. During compression, the fiber volume fraction increased, which induced a rise in the volumetric heat capacity of the system. Although the heat capacity per unit mass of the fabric was approximately that of the solid, the same did not apply for the heat capacity per unit volume because the volume of air

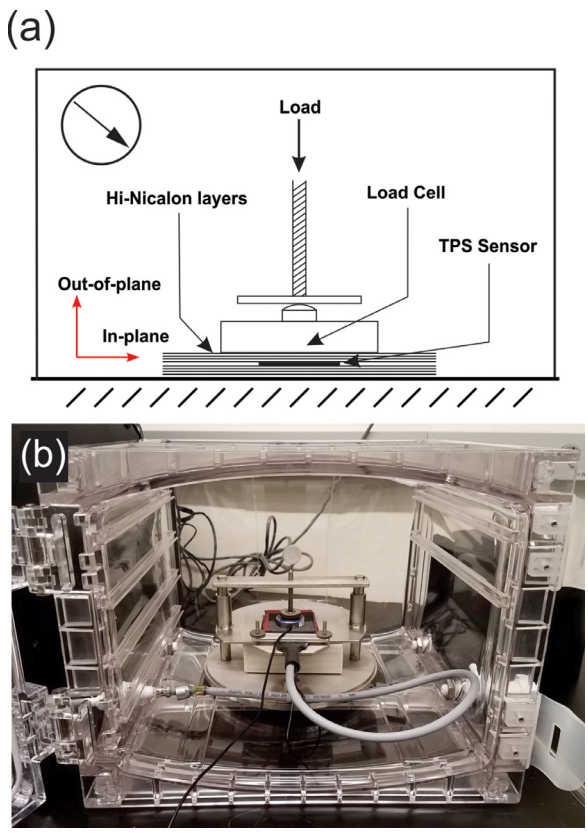

Fig. 2. Experimental thermal conductivity characterization using the hot-disk transient plane source method under controlled air pressure conditions. (a) Sketch of the set up. (b) Optical image of the vacuum cabinet and hot disk sample holder.

represented 55-70% of the representative volume element (RVE), as will be discussed later in Section 4.1. Subsequently, thermal conductivity measurements were corrected at each loading condition. To make this correction, we used the fiber volume fraction computed in compression by FEA, because direct measurement is not feasible experimentally. It may be argued that the compression strain predicted by FEA could underestimate the actual experimental value. For this reason, the bridge between experiment and FEA model was done through the compression stress, calculated from the applied transverse load in the experiment and reaction force in the model. It is assumed that both experiment and model produce same deformation under an identical compressive stress. Therefore, for each measurement, V_{fiber} was calculated computationally from the percentage of compression strain that yields the same stress as that in the experiment.

To study the effect of air pressure in the thermal conduction of the fabric, the sample holder was mounted inside a vacuum cabinet (F42400-4021, Bel-Art SP Scienceware, NJ, USA) (Fig. 2(b)), (29inHg vacuum for 72hr capacity). Hi-Nicalon and heat-cleaned Nextel-BF20 samples were tested under the same conditions. A sensor of 6.4 mm radius was used to perform the measurements. To prevent air leaks, epoxy resin was used to seal the cable of the hot-disk sensor. A ply of 4 fabric samples was used at each side of the sensor. The optimum recording time and output power were determined through an iterative process. A transient recording time of 10s and an output power of 40 mW were used in this study for both materials. Starting from an un-loaded state, the thermal conductivity was measured at 1 and 0.16 atm before an increase in compressive stress, 3 thermal conductivity measurements were executed for each data point. To ensure the system returned to thermal equilibrium and mechanical relaxation, wait times of

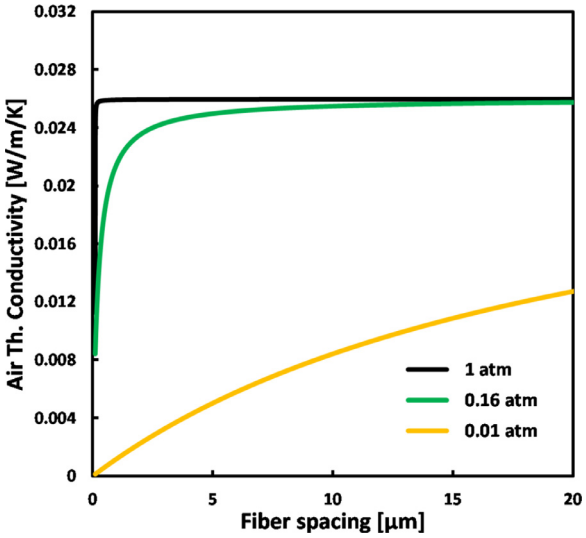

Fig. 3. Thermal conductivity of air as a function of confinement spacing for an air pressure of 1, 0.16 and 0.01 atm.

30 minutes were used between measurements. Room temperature conditions remained constant at 23 ± 1 °C.

3. Micro-level intra-yarn heat-transfer

3.1. Proposed finite-element model

It has been shown that to represent the thermal behavior of confined air in micro spacings, as a function of pressure and temperature, the air thermal conductivity K_{air} must be corrected such as [3],

$$K_{air} = \frac{K_{air0}}{1 + 2\frac{(2-\alpha)2\gamma}{\alpha(\gamma+1)}\frac{1}{Pr}Kn} \tag{3}$$

where K_{air0} is the thermal conductivity of free air, α is an accommodation coefficient that characterizes the behavior of a gas particle in the collisions with a solid and varies between 0 and 1 [3], $\gamma = C_p/C_v$ is the adiabatic coefficient or heat capacity ratio, Pr is the Prandtl number and Kn is the Knudsen number, given by the expression:

$$Kn = \frac{\lambda}{L_c} = \frac{k_B T}{\pi\sqrt{2} d_g{}^2 P L_c} \tag{4}$$

Here, λ is the molecular mean free path length, k_B is the Boltzmann's constant, T is the gas temperature, d_g is the diameter of the gas molecule, P is the pressure, and L_c is the characteristic length. The Knudsen number is defined as the ratio between the molecular mean free path length of a gas to a characteristic physical length and indicates whether a continuum or kinetics theory of gases should be applied. When the characteristic length approaches the molecular mean free path and $Kn > 0.1$, continuum theory is no longer applicable, and the thermal conductivity should be corrected by using Eq. (3) [3]. The characteristic length L_c for fibrous insulations is typically approximated by the characteristic pore length as [12],

$$L_c = \frac{\pi D_{fiber}}{4V_{fiber}} \tag{5}$$

where D_{fiber} is the fiber diameter. Here, we will use L_c to model the micro-spacing between fibers. Fig. 3 represents the theoretical value of air thermal conductivity, as a function of spacing L_c, obtained for different P pressures by combining Eqs. (3)-(5).

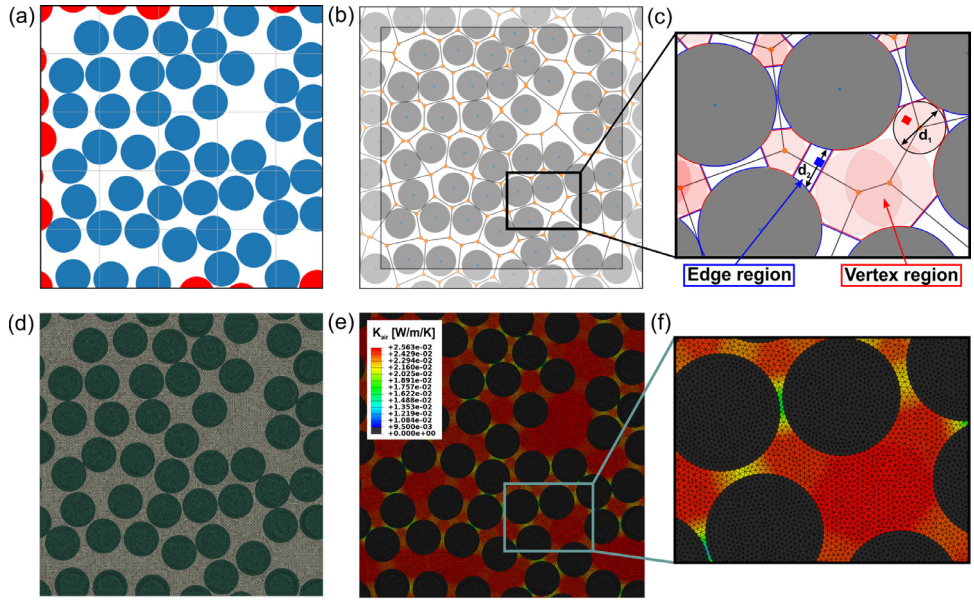

Fig. 4. Intra-yarn RVE thermal modeling. (a) Randomized periodic structure of fibers. (b) Voronoi cell structure of the RVE and (c) gap size method for local assignment of thermal conductivities. (d) Finite element mesh of the intra-yarn RVE. (e) Air thermal conductivity map of the periodic RVE, and (f) close view of the intra-yarn thermal conductivity map.

A 3D FEA model of the fibrous structure was created to accurately study the heat conduction at the microscale inside yarns. SEM analysis of the yarn structure shown in Fig. 1(c) and (d) indicated that the fibers were mostly parallel to each other with a random cross-sectional distribution. Therefore, following this observation, our RVEs were constructed in 2D with periodic boundaries and different V_{fiber} = 45, 50, 55 and 60%. To this end, a Discrete Element Method (DEM) solver was coded to generate a random fiber distribution. A set of 49 fibers with a prescribed radius were placed in the plane with a square packing structure. The fibers were positioned at equidistance to produce the exact fiber volume fraction. The elements (fibers) were given random forces and the simulation box had periodic boundaries. A penalty contact property was established between them and the simulation was left to run to produce a random fiber distribution. Fig. 4 (a) shows the result of this simulation, where in blue are the simulated fibers, and in red the periodic counterparts inside the simulation box. The fiber distribution was imported to ABAQUS [25] afterwards and meshed. Diffusive tetrahedral elements were used with a size of 0.5 µm. The Hi-Nicalon fibers and Nextel-440 fibers were modeled using cylinders with D_{fiber} = 14 µm, and 12 µm, respectively. The space occupied by air was modeled as a fluid matrix.

To properly assign a conductivity value to air elements according to their L_c, the air region was spatially parametrized using a Voronoi cell structure as shown in Fig. 4(b). On each Voronoi vertex, a pore space was defined as the largest circle, centered at the vertex, without fiber material (Fig. 4(c)). A characteristic length (L_c) equal to the diameter of the circle was assigned to the pore. The air space was divided in 2 region types: “vertex” region (red color in Fig. 4(c)) was the space where the pores covered the Voronoi cell boundaries, and “edge” region (blue color in Fig. 4(c)) the remaining space within fibers. If an air element centroid was in the “vertex” region, the thermal conductivity was calculated using the characteristic length of the pore that contained the element (d_1 in Fig. 4(c)), the largest characteristic length if it lied in more than one pore, and the characteristic length of the closest pore if it was not contained by any pore. On the other hand, if an element centroid was in the “edge” region, L_c was calculated as the length of the line, perpendicular to the Voronoi cell boundary, that goes through the centroid of the element and connects both fibers (d_2 in Fig. 4(c)). The thermal conductivity was then computed for all the air elements in the RVE, the resulting model accounted for micro-spacing effects in between fibers as well as any variation in pressure as shown in Figs. 4(e) and (f).

A 296 K predefined temperature field was established as initial condition. A temperature gradient of 5 K was applied as the boundary condition, keeping the rest of the surfaces insulated. Due to the low temperatures and low gradients, radiation effects were considered negligible. Air was considered stagnant within the porous structure, therefore only thermal transport through conduction was contemplated.

Material properties were modeled by heat-transfer user-defined material subroutines (UMATHT) in ABAQUS. The thermal conductivities of the fibers were those estimated from experiments, as discussed above. Air thermal conductivity properties were calculated for pressures of 1 atm, 0.16 atm and 0.01 atm using Eqs. (3) and (5).

The steady-state heat conduction was calculated using Fourier’s law:

$$Q = -K_{eff} A \frac{\Delta T}{\Delta x} \tag{6}$$

where Q is the computed heat flow, K_{eff} is the effective thermal conductivity, A was the cross-sectional area of the RVE, ΔT was the temperature gradient, and Δx was the dimension of the RVE.

Two RVE structures were made for each volume fraction. Each structure was run twice, with the temperature gradient placed in the vertical and horizontal directions. A total of 4 simulations per volume fraction were computed and the final K_{eff} value was averaged. An exponential curve was fitted to get an expression for the transverse thermal conductivity as a function of volume fraction.

3.2. Model sensitivity to fiber volume fraction

Microscopic level yarn models were generated for various volume fractions of fiber and their effective thermal conductivity was simulated by steady-state heat-transfer FEA in both Hi-Nicalon and Nextel-440 yarns at different gas pressures. Fig. 5 (a) and (b) show

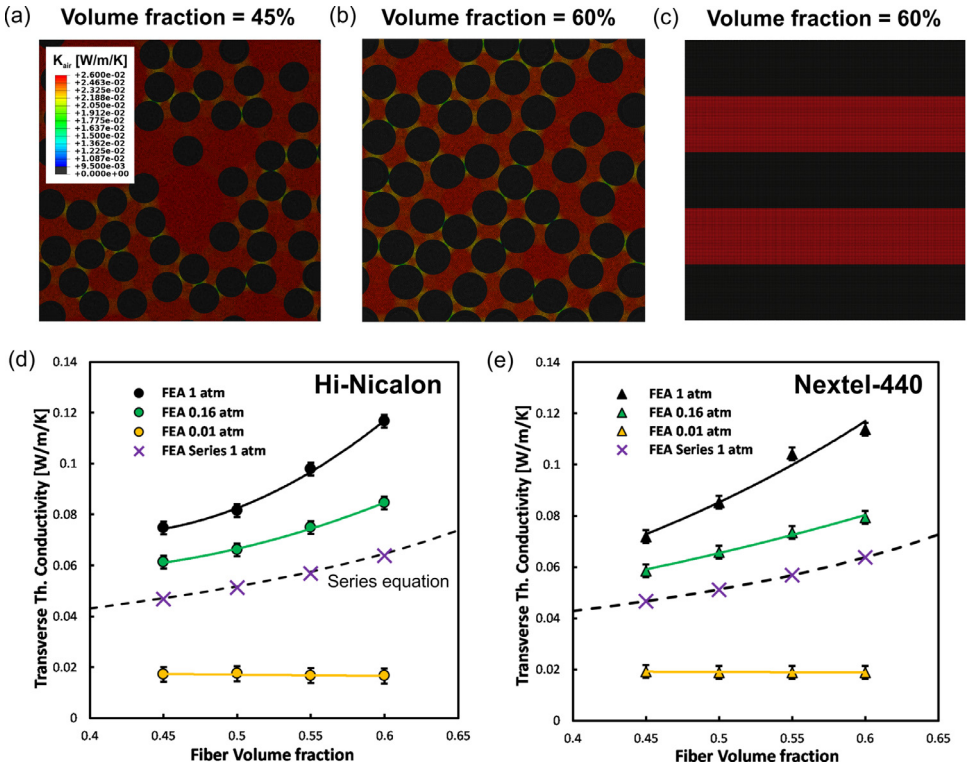

Fig. 5. Intra-yarn steady-state heat transfer finite element analysis. (a)-(b) RVE models of a Hi-Nicalon yarn with 45 and 60% volume of fiber, respectively. (c) FEA series model. (d) Simulated transverse thermal conductivity of a Hi-Nicalon yarn as a function of fiber volume fraction. (e) Simulated transverse thermal conductivity of a Nextel-440 yarn as a function of fiber volume fraction. The dashed black lines represent the solution of the analytical series equation for confined air at 1 atm, which matches with the results of the FEA series model.

the thermal conductivity map for a Hi-Nicalon yarn at 1 atm with a fiber volume fraction of 45 and 60% respectively. For comparison, Fig. 5(c) shows a FEA series model for Hi-Nicalon at 1 atm and a fiber volume fraction of 60%. In the series model, air thermal conductivity was given by the combined Eqs. (3)-(5). Boundary conditions, element type, step and property extraction remained unaltered.

The FEA simulation results for the transverse thermal conductivity in Hi-Nicalon and Nextel-440 models are represented in Figs. 5(d) and (e), respectively. In addition to the micro-scale intra-yarn simulations, these figures show the solution of a standard heat-conduction series model for both materials at 1 atm predicted by FEA (cross symbols) and analytically (dashed line) with K_{air} obtained from Eqs. (3)-(5). Both FEA and analytical solutions for the series model are in excellent agreement. Interestingly, however, the new transverse thermal conductivity predicted by the proposed FEA model at 1 atm is higher than the series solution at all V_{fiber} studied, and its dependence on V_{fiber} is more pronounced. With an increase in V_{fiber} from 45% to 60%, the conductivity rises by 35% with the series model, while the proposed model reaches a 55% increase in conductivity for Hi-Nicalon and a 60% increase for the Nextel-440 model. Apparently, the volume fraction dependence also exhibits a more linear trend for the Nextel model than the Hi-Nicalon one.

Furthermore, the difference in the response of the FEA model to variations in fiber thermal conductivity was found to be negligible. The computed standard deviation was found to be less than 0.003 W/m/K. The model results, however, reveal a higher sensitivity to slight changes in fiber diameter (14μm in Hi-Nicalon to 12μm in Nextel-440). For the range of thermal conductivities and length scales that are presented in this study, the model response is primarily controlled by the geometry and air thermal properties.

3.3. Model sensitivity to air pressure

We find that the increase in thermal conductivity with increasing V_{fiber} becomes less significant as air pressure is decreased. For instance, a conductivity reduction of 15% to 20% is observed for $V_{fiber} = 45\%$ when pressure drops from 1 atm to 0.16 atm, whereas a larger reduction of 25% to 30% is observed for $V_{fiber} = 60\%$. This phenomenon can be attributed to the result in Fig. 3 showing that the sensitivity of air thermal conductivity to micro-scale spacing increases significantly when pressure is reduced from 1 atm to 0.16 atm. In fact, for an air pressure of 0.01 atm, we find in Fig. 5(d) and (e) that the microscale FEA predictions yield a constant transverse thermal conductivity of only 0.017 W/m/K, a reduction by almost one order of magnitude with respect to the predictions at 1 atm.

Fig. 6 shows the effect of air pressure on the local air thermal conductivity for a Nextel-440 yarn with a fiber volume fraction of 45% and 60%, respectively. At 1 atm, most of the pore structure (vertex regions) conserves a thermal conductivity close to that of free air (0.026 W/m/K), the effect of air confinement is only relevant for narrow edge regions were fibers are nearly in contact. At 0.16 atm, all edge regions display a significant drop in thermal conductivity, while thermal conductivity in vertex regions are still relatively high, especially in those with a high characteristic length. At 0.01 atm, we can observe that the computed thermal conductivity in the edge regions is an order of magnitude lower compared to that of free air. The vertex regions suffer now a general significant decrease in thermal conductivity. A comparison of Figs. 6(a) and (b) suggests that an increase in V_{fiber} tends to increase the amount of edge regions at the expense of the amount and size of vertex regions, where Knudsen effects are less pronounced. Therefore, the increase in V_{fiber} has a smaller influence on the overall thermal

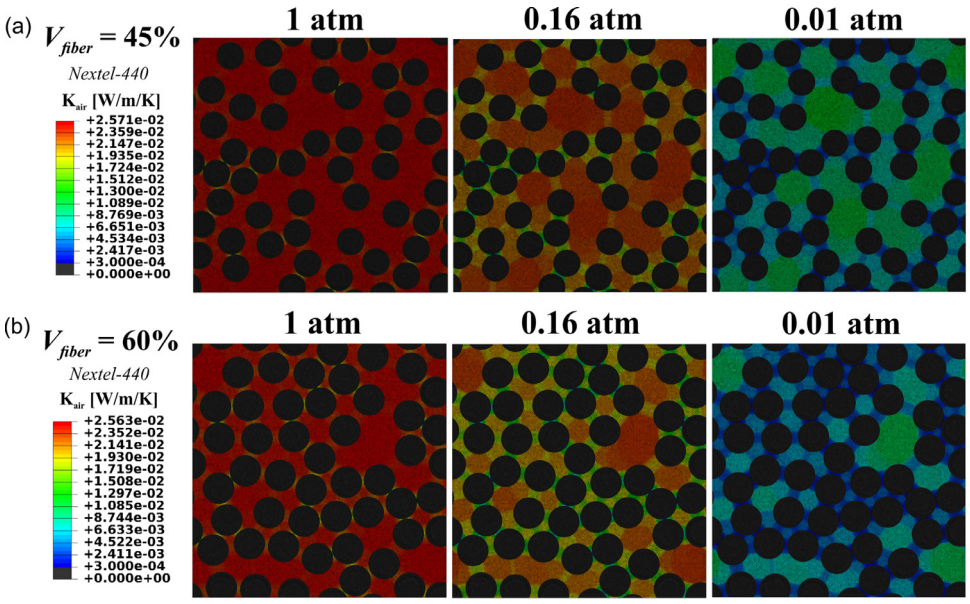

Fig. 6. Nextel-440 intra-yarn model air thermal conductivity maps for an air pressure of 1, 0.16 and 0.01 atm for: (a) yarn with 45% fiber volume fraction, and (b) yarn with 60% fiber volume fraction.

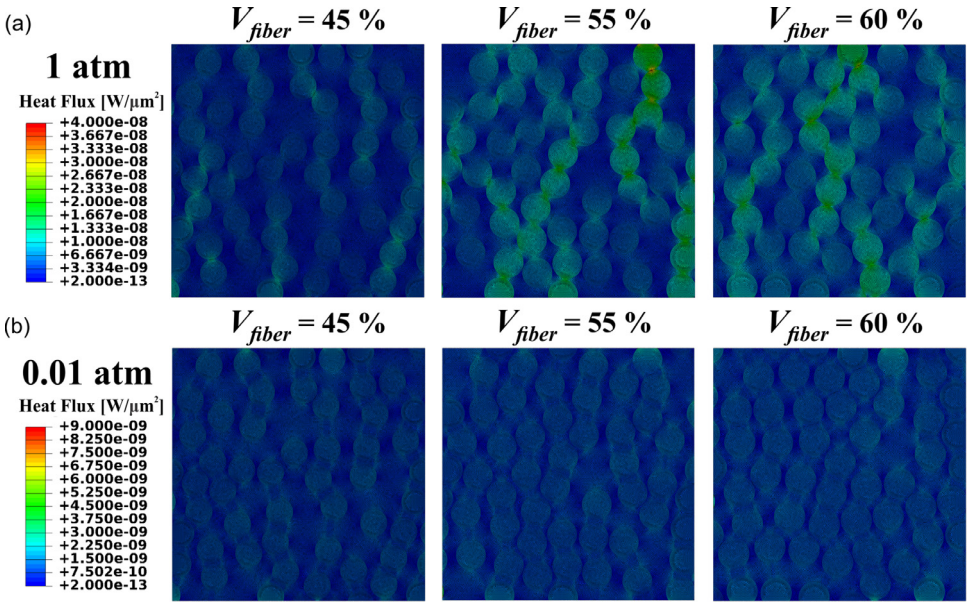

Fig. 7. Nextel-440 intra-yarn model heat flux maps for a volume fraction of 45, 55 and 60% at different air pressure: (a) 1 atm, and (b) 0.01 atm.

conductivity when pressure decreases, as predicted in Fig. 6(d) and (e).

Fig. 7 represents the effect of air pressure over the local heat flux for a Nextel-440 yarn as a function of fiber volume fraction. This figure shows that, at 1 atm, the heat flux finds preferential paths through the fibers and edge regions in the direction of the temperature gradient (vertical) as the volume fraction is increased, promoting the increase in effective thermal conductivity shown in Fig. 5(e). A preferential path forms, despite the conductivity reduction in the narrow edge regions, because this reduction is not large enough to counter the effect of fibers getting closer (the thermal conductivity of the fibers is 2 orders of magnitude higher). By contrast, at 0.01 atm, we observe that the heat flux remains uniform with increasing fiber volume fraction. The reduction from 1 atm to 0.01 atm greatly increases the effect of micro-spacing confinement (Fig. 3). As a result, all edge regions have now a small thermal conductivity value at 0.01 atm in Fig. 6. Consequently, there is a larger resistance for the heat flux to form a preferential path at 0.01 atm than at 1 atm. Therefore, this result allows us to conclude that air thermal conductivity for a pressure of 0.01 atm strongly controls the behavior of the model. Hi-Nicalon was found to exhibit the exact same behavior.

4. Mesoscale woven fabric model

4.1. Woven fabric modeling and mechanical behavior

Due to their periodic structure, Nextel-BF20 and Hi-Nicalon fabrics were modeled with a minimum representative volume element (RVE) as shown in Figs. 8 (a) and (b), respectively. Their geometry was determined by scanning electron microscopy (SEM). The geometry of the RVE was generated using the software TEX-

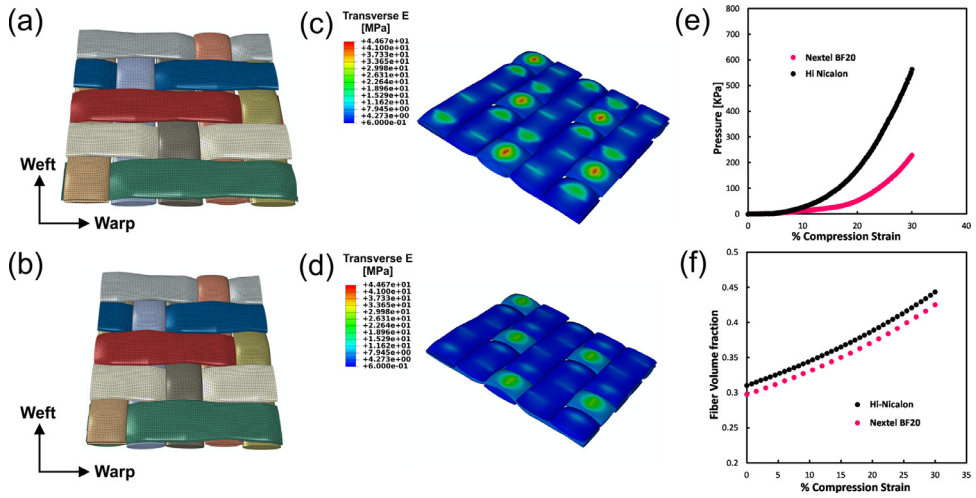

Fig. 8. Representative volume element (RVE) mechanical model. (a) Hi-Nicalon 5HS woven fabric RVE. (b) Nextel-BF20 woven fabric RVE. (c) Transverse Young's modulus map of Hi-Nicalon at 30% compression strain. (d) Transverse Young's modulus map of Nextel-BF20 at 30% compression strain. (e) Mechanical compression pressure as function of compression strain for Hi-Nicalon and Nextel-BF20. (f) Fiber volume fraction of the RVE as a function of compression strain for Hi-Nicalon and Nextel-BF20.

GEN [24] and exported to the FEA software ABAQUS [25]. A local coordinate system was created in every element to represent the longitudinal and transversal directions of the fibers within the yarns. The production of the finite element models is further discussed in our previous work [2].

Hi-Nicalon 5HS was found to be a well-balanced fabric, with the same amount of fiber count per unit length in the warp and weft directions. The dimensions of the RVE before compression were $5 \times 5 \times 0.5$ mm^3. By contrast, Nextel-BF20 was found to be a non-balanced fabric. Although the nominal count of fibers per yarn was the same for the warp and weft directions, the count per unit length was different, because of the yarns compressed in the warp direction as shown in Fig. 8(b). The dimensions of the RVE before compression were $4.15 \times 5 \times 0.55$ mm^3.

A mechanical constitutive law developed by Lin et al. [26] was implemented through a user material subroutine to model the mechanical behavior under transverse loading. The yarn was treated as a transversely isotropic material with a longitudinal Young's modulus given by $E_{11} = E_{fiber}V_{fiber}$ and a transverse modulus obtained by [2,26]:

$$E_{22}(\epsilon_{22}) = \frac{\sigma_{22}}{\epsilon_{22}} = \frac{-a\left(\frac{V^0_{fiber}}{\exp(\epsilon_{22})}\right)^b + a\left(V^0_{fiber}\right)^b}{\epsilon_{22}} \tag{7}$$

Here, a and b are experimental parameters that depend on the initial configuration and arrangement of fibers prior to compression. For simplicity, a and b are taken as constant with values of 1151 and 12.24, respectively, as suggested in Ref. [26]. $\sigma_{22} = \sigma_{33}$ is the stress in the transverse direction and $\epsilon_{22} = \epsilon_{33}$ the corresponding strain. V^0_{fiber} represents the initial fiber volume fraction of the element. The mechanical compression modeling is further developed in Ref. [2].

A 30% compression strain simulation was performed for both models. Fig. 8(e) shows the evolution of compressive stress as a function of applied compressive strain. The Hi-Nicalon model exhibited a higher increase in compressive stress after an 8% strain than Nextel, reaching a pressure of 563.5 KPa at the end of the simulation. The pressure in the Nextel model evolved at a slower pace to reach 229.7 KPa. Figs. 8(c) and (d) show the local transverse Young's modulus through the geometry of the RVEs at 30% compression. Both models exhibited stiffening on the spots where the yarns are woven. The Nextel RVE produced a larger overall Young's modulus through the warp yarns when compared to the weft yarns. No major difference in modulus was found between weft and warp yarns for the Hi-Nicalon RVE.

The variation of volume fraction in the RVE with compression was determined under the assumption that the total volume of fibers remained constant through the compression. As discussed in Section 2, only the compression stress was measured during the hot-disk experiment. The volume fractions used to revise the volumetric heat capacity were obtained by mapping the reaction loads in the simulation and experiment. Each experimental measurement was performed at a specific compression stress, which was mapped to the computational compression strain in Fig. 8(e). Then, the volume fraction was extracted from the strain using the relation shown in Fig. 8(f).

From the mechanical compression simulation, the mean yarn volume fraction was found to vary between 0.4748 and 0.5327 for the Hi-Nicalon model, and between 0.4933 and 0.5183 for the Nextel-BF20 model.

4.2. Meso-level woven fabric out-of-plane thermal conductivity

A steady-state heat transfer simulation on the out-of-plane direction was performed at every 1.5% compression over the fabric RVE following the methodology described in Ref [2]. Two heat transfer constitutive models were used to describe the thermal behavior of the yarn. First, the standard series model was used together with combined Eqs. (3)-(5), i.e. the black dashed lines in Figs. 5(d) and (e). Second, we used the proposed multiscale approach, where the transverse effective thermal conductivity of the yarn was given by the micro-scale yarn simulation results in Fig. 6. The longitudinal thermal conductivity of the yarn was approximated by combining a parallel model and Eqs. (3)-(5). The material behavior was implemented using a user material subroutine UMATHT.

The air within the yarn structure was modeled with a gap thermal conductance. This surface-to-surface element interaction was defined as:

$$Cond = \frac{K_{air}}{L_c} \tag{8}$$

where K_{air} is given by Eq. (3), and the characteristic length L_c represents the spacing between two yarns. The evolution of the gap thermal conductance as a function of L_c is represented in Fig. 9.

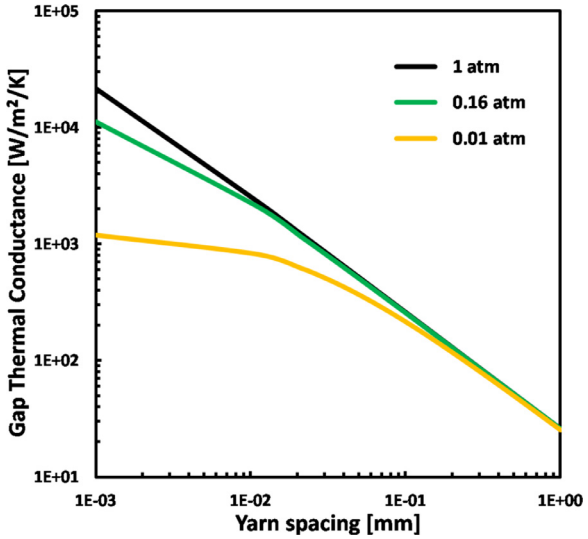

Fig. 9. Thermal conductance of air between the yarns as a function of yarn spacing for an air pressure of 1, 0.16 and 0.01 atm.

4.3. Experimental validation on Nextel-BF20 and Hi-Nicalon woven fabrics

Figs. 10 (a) and (b) show a comparison between the transient plane source measurements and the out-of-plane FEA results. It can be observed that the proposed multiscale computational approach successfully captures the effect of compressive stress and atmospheric pressure over the fabric out-of-plane thermal conductivity, for both types of fabrics. Furthermore, Fig. 10 indicates that the series model (dashed lines) does not produce accurate results. A series model underestimates the effective thermal conductivity at 1 atm and 0.16 atm, compared to the multiscale approach, and overestimates it at 0.01 atm. This finding reveals that modelling the yarn as resistances placed in series and averaging the pore size, as shown in Eq. (5), is not an effective solution to capture the thermal behavior of woven fabrics under variable air pressures.

Figs. 10(a) and (b) show that the overall out-of-plane behavior of Hi-Nicalon and Nextel-BF20 at room temperature are similar. The thermal conductivity of the fibers is close, 8 W/m/K for Hi-Nicalon and an approximate range of 5 to 7 W/m/K for Nextel-440 fibers. Although both bulk silicon carbide and alumina have much higher conductivity [23,28], the nanocrystalline structure of Hi-Nicalon [23] and the silicon oxide and glassy phases present in Nextel fibers [14] reduce the fiber conductivity by one order of magnitude. Furthermore, from our FEA simulations, the Nextel-440 yarn model did not exhibit any significant change when the conductivity of the fiber was set from 7 to 5 W/m/K, which suggests that the few differences in magnitude between the Hi-Nicalon yarn and the Nextel yarn are driven by the geometry only.

Qualitatively, from the shape and evolution of the measurements with compressive stress, we find that the Hi-Nicalon fabric differs noticeably from the Nextel-BF20 one. In Fig. 10, the Nextel fabric shows 3 distinguishable regimes: A sudden jump in conductivity in the beginning of the curve that was associated to a jump-to-contact in the yarns during compression, a second regime were conductivity increases due to gaps closing and yarn densification, and a third region after 30KPa with a softer increase in conductivity where all that is observed is densification of the yarns. These 3 regimes are present for all studied vacuum levels and are the same as those identified in our previous study [2]. Hi-Nicalon, however, does not show a second transition. After the gap overclosure at the beginning, the conductivity increases with no sudden change

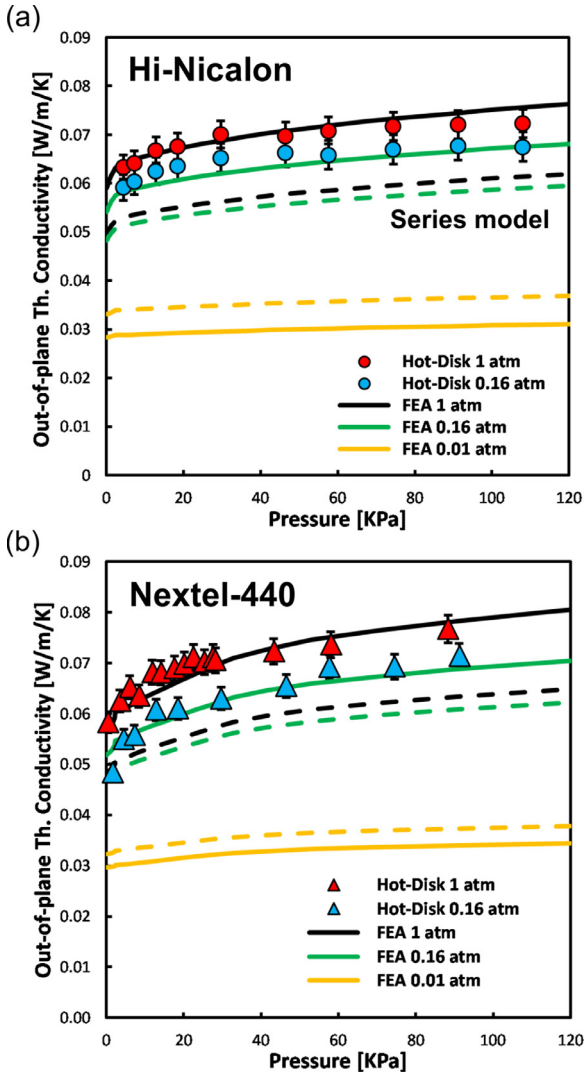

Fig. 10. Simulated out-of-plane thermal conductivity compared to the hot-disk transient plane source measurements under compressive strain, for (a) Hi-Nicalon 5HS fabric and (b) Nextel-BF20 fabric. The dashed lines represent the simulation results using the series model for the transverse thermal conductivity of the yarn.

in slope. We attribute this behavior to the more regular and balanced structure of the Hi-Nicalon 5HS fabric.

5. Discussion

5.1. Effect of gas pressure in the out-of-plane thermal conductivity of woven fabrics

Out-of-plane thermal conductivity in woven fabrics is clearly influenced by gas pressure as evidenced in Fig. 10, both computationally and experimentally. The Knudsen correction to the gas conductivity described by Eq. (3) is demonstrated to be essential to understand this behavior. Figs. 3 and 9 reveal the gas pressure dependence of thermal conductivity and thermal conductance, respectively, for stagnant air in micro-spacing. A direct response for this behavior is manifested in Fig. 6 where it is found that a decrease in pressure dramatically reduces air thermal conductivity, especially in the edge regions where the characteristic length is smaller. Results in Figs. 6 and 7 point to the conclusion that the Knudsen effect controls the heat transfer through conduction inside the yarns. By lowering the gas pressure, the mean free path

of the air molecules increases while the characteristic length of the confinement remains the same or even is reduced with compressive strain. Consequently, the gas not only reduces its conductivity through the entire porous structure, but also large resistances are created in the edge regions, preventing heat flux to have a preferential path. A similar effect is most likely possible in yarn-to-yarn contacts as well.

5.2. Multiscale approach versus series formulation

Fig. 10 provides clear evidence that the multiscale approach proposed in this study quantitatively captures the behavior and magnitude of the experimental measurements, as opposed to the commonly used series model. Although the latter qualitatively fits the trend and shape of the curve, it fails to predict the magnitude for all vacuum levels tested. This result is important in different aspects. First, the series arrangement of a group of resistances or conductances represent the lower bound of effective overall conductivity for the system, while the parallel arrangement is the upper bound. Therefore, in the series model (Fig. 5(c)), it is assumed that the heat flux through the system is homogeneous with no preferential path and must go through the air. A concrete example to understand the importance of the preferential path is found in Fig. 7. As explained in the previous section, the heat flux increases with volume fraction at 1 atm because preferential paths are found. On the contrary, at 0.01 atm, the same increase in volume fraction does not produce an increase in heat flux. As more realistic yarn structures contain networks of preferential heat paths, the series formulation will always underestimate the effective conductivity value.

Second, the geometry of the system is not correctly taken into account by the series formulation. To implement the Knudsen effect into the series model, a value of the characteristic length as a function of fiber volume fraction is used as given by Eq. (5). Consequently, a constant pore size is being used, which neglects the effects of high thermal resistances that appear on the edge regions.

Finally, the multiscale formulation allows for further implementation of physical phenomena such as oxidation or phase changes in the fiber material or the study of thermal contact resistances. The effect of thermal contact resistances should increase for high volume fractions near ideal close-packed fiber arrangements, due to the increase in fiber-to-fiber contacts, and play a critical role at ultra-high vacuum levels where conduction through the fibrous network and thermal radiation are the main heat carriers. Here, heat constriction resistances could possibly limit the heat flow through the network [27].

5.3. Model limitations

To be able to perform the mechanical compression step, the air matrix around the yarn was removed and substituted by a gap thermal conductance property (Fig. 9) [2]. This property is a surface-to-surface contact interaction that works well between close-to-parallel surface meshes, but also is not guaranteed to be reliable otherwise. This, together with the suppression of air elements in the in-plane boundaries of the RVE, prevented us to correctly apply the necessary boundary conditions and output requests to compute the effective in-plane thermal conductivity by FEA. The use of conjugate heat-transfer methods [29-31] may be able to solve this problem.

Furthermore, at the yarn level, assuming a perfectly parallel arrangement of fibers may be overestimating the longitudinal value in the same fashion that the series model underestimates the transverse value.

6. Conclusions

A multiscale thermo-mechanical FEA model was created to simulate and study the evolution of the out-of-plane thermal conductivity with different strain and gas pressures in 2D woven ceramic fabric materials. Nextel-BF20 and Hi-Nicalon 5HS fabric materials were modeled and their thermal conductivity was computed, as a function of compressive stress, for air pressures between 1 atm, 0.16 atm and 0.01 atm. The results were validated through experimental measurements at 1 atm and 0.16 atm using the hot-disk transient plane source technique. The following major conclusions can be drawn from the present study:

- The out-of-plane thermal conductivity in 2D woven fabric materials decreases with the decrease of pressure due to Knudsen effects in micro-spacings. We observe that not only the magnitude is reduced, but also the dependence on compression stress falls as pressure decreases. This is attributed to a pronounced decrease in air conductivity in the spacing between fibers that prevents the formation of preferential heat flow paths as the fiber volume fraction increases.
- The FEA multiscale approach proposed and the transient plane source measurements showed excellent agreement for both Nextel-BF20 and Hi-Nicalon fabrics. The series formulation for transverse yarn thermal conductivity, however, produced inaccurate results. This finding suggests that a proper geometry at the micro-level, inside the yarn, is essential to accurately capture the thermal behavior of the material in the meso-level.

This study shows that the proposed methodology is applicable to the out-of-plane thermal conductivity of woven fabrics under compressive stress and variable atmospheric gas pressure. This new microscopic model could be used to improve the computational analysis of anisotropic effective conductivity in fibrous and woven materials [32,33] or help study other complex temperature-dependent phenomena such as the oxidation of Hi-Nicalon fabrics under mechanical stress [34]. This multiscale approach could also be adapted for modeling complex dynamical loads [35] and different woven materials relevant for the development of future flexible TPS.

Declaration of Competing interest

The authors declare that they have no known competing financial interests or personal relationships that could have appeared to influence the work reported in this paper.

CRediT authorship contribution statement

Rodrigo Penide-Fernandez: Conceptualization, Methodology, Software, Validation, Formal analysis, Investigation, Visualization, Writing – original draft. **Frederic Sansoz:** Conceptualization, Methodology, Resources, Writing – original draft, Supervision, Funding acquisition.

Acknowledgements

Support received by the NASA EPSCoR Program under NASA Cooperative Agreement No. NNX14AN20A and No. NNX15AK55A is gratefully acknowledged. We also gratefully thank Dr. Anthony Calomino of NASA Langley Research Center for providing the Hi-Nicalon woven fabric materials tested in this work.

References

[1] J. Del Corso, F. Cheatwood, W. Bruce, S. Hughes, A. Calomino, Advanced high-temperature flexible TPS for inflatable aerodynamic decelerators, 21st AIAA Aerodyn, Decelerator Syst, Technol. Conf. Semin. (2011) 1–23.

[2] R. Penide-Fernandez, F. Sansoz, Anisotropic thermal conductivity under compression in two-dimensional woven ceramic fibers for flexible thermal protection systems, Int. J. Heat Mass Transf 145 (2019) 118721.
[3] M.G. Kaganer, Israel Program for Scientific Translations, Thermal Insulation in Cryogenic Engineering (1969).
[4] M. Bahrami, M.M. Yovanovich, J.R. Culham, Effective thermal conductivity of rough spherical packed beds, Int. J. Heat Mass Transf. 49 (2006) 3691–3701.
[5] J. Kwon, C.H. Jang, H. Jung, T. Song, Effective thermal conductivity of various filling materials for vacuum insulation panels, Int. J. Heat Mass Transf 52 (23–24) (2009) 5525–5532.
[6] J.J. Zhao, Y.Y. Duan, X.D. Wang, B.X. Wang, Effects of solid-gas coupling and pore and particle microstructures on the effective gaseous thermal conductivity in aerogels, J. Nanoparticle Res. 14 (8) (2012) 1024.
[7] D.S. Smith, A. Alzina, J. Bourret, B. Nait-Ali, F. Pennec, N. Tessier-Doyen, K. Otsu, H. Matsubara, P. Elser, U.T. Gonzenbach, Thermal conductivity of porous materials, J. Mater. Res. 28 (2013) 2260–2272.
[8] A. Das, R. Alagirusamy, P. Kumar, Study of heat transfer through multilayer clothing assemblies: A 11 (2011) 54–60.
[9] M. Fu, M.Q. Yuan, W.G. Weng, Modeling of heat and moisture transfer within firefighter protective clothing with the moisture absorption of thermal radiation, Int. J. Therm. Sci. 96 (2015) 201–210.
[10] K. Daryabeigi, Thermal Analysis and Design of Multi-layer Insulation for Re-entry Aerodynamic Heating, in: 35th AIAA Thermophysics Conference 11-14 June 2001 Anaheim, Aerospace, 2001, pp. 1–8.
[11] K. Daryabeigi, G.R. Cunnington, S.D. Miller, J.R. Knutson, Combined Heat Transfer in High-Porosity High-Temperature Fibrous Insulations: Theory and Experimental Validation, J. Thermophys. Heat Tr. 25 (2011) 536–546.
[12] S.Yuan Zhao, B.Ming Zhang, X.Dong He, Temperature and pressure dependent effective thermal conductivity of fibrous insulation, Int. J. Therm. Sci. 48 (2) (2009) 440–448.
[13] S.A. Lurie, Y.O. Solyaev, D.V. Lizunova, L.N. Rabinskiy, V.M. Bouznik, O. Menshykov, Influence of mean distance between fibers on the effective gas thermal conductivity in highly porous fibrous materials, Int. J. Heat Mass Transf 109 (2017) 511–519.
[14] Duan Li, Bin Li, Yuanyi Zheng, Shitao Gao, Xuejin Yang, On the mechanical, thermophysical and dielectric properties of Nextel™ 440 fiber reinforced nitride matrix (N440/Nitride) composites, Ceramics International 44 (6) (2018) 6137–6143.
[15] E.L. Christiansen, B.Alan Davis, Heat-Cleaned Nextel in MMOD Shielding, First Int'l. Orbital Debris Conf, 2019 Conference Paper.
[16] D.J. Duval, S.H. Risbud, J.F. Shackelford, Mullite, 2008.
[17] D. Schawaller, B. Clauß, M.R. Buchmeiser, Ceramic filament fibers - A review, Macromol. Mater. Eng. 297 (2012) 502–522.
[18] R. Yamada, N. Igawa, T. Taguchi, S. Jitsukawa, Highly thermal conductive, sintered SiC fiber-reinforced 3D-SiC/SiC composites: experiments and finite-element analysis of the thermal diffusivity/conductivity, Journal of Nuclear Materials 307–311 (2) (2002) 1215–1220.
[19] Y. He, Rapid thermal conductivity measurement with a hot disk sensor: Part 1. Theoretical considerations, Thermochim. Acta. 436 (1) (2005) 122–129.
[20] S.E. Gustafsson, Transient plane source techniques for thermal conductivity and thermal diffusivity measurements of solid materials, Rev. Sci. Instrum. 62 (1991) 797–804.
[21] M. Gustavsson, H. Nagai, T. Okutani, Characterization of anisotropic and irregularly shaped materials by high-sensitive thermal conductivity measurements, , Solid State Phenom 124–126 (2007) 1641–1644.
[22] N.K. Michael, G. Miller, Jason M. Keith, Julia A. King, Brian J. Edwards, Measuring thermal conductivities of anisotropic synthetic graphite-liquid crystal polymer composites, Polym. Compos. 27 (4) (2006) 388–394.
[23] B. Zhu, R. Wang, S. Harrison, K. Williams, R. Goduguchinta, J. Schneiter, J. Pegna, E. Vaaler, X. Wang, Thermal conductivity of SiC microwires: Effect of temperature and structural domain size uncovered by 0 K limit phonon scattering, Ceram. Int. 44 (2018) 11218–11224.
[24] H. Lin, L.P. Brown, A.C. Long, Modelling and Simulating Textile Structures Using TexGen, Adv. Mater. Res. 331 (2011) 44–47.
[25] ABAQUS 2018Dassault Systèmes Simulia Corp., 2017 Johnston, RI, USA.
[26] H. Lin, M. Sherburn, J. Crookston, A.C. Long, M.J. Clifford, I.A. Jones, Finite element modelling of fabric compression, Model. Simul. Mater. Sci. Eng. 16 (3) (2008).
[27] Chuan-Yong Zhu, Zeng-Yao Li, Modeling of the apparent solid thermal conductivity of aerogel, Int. J. Heat Mass Transf. 120 (2018) 724–730.
[28] P. Auerkari, Mechanical and physical properties of engineering alumina ceramics, Technical Research Centre of Finland, VTT Manufacturing Technology, Research Notes 1792 (1996) 3–36.
[29] D.J. Lopez Penha, S. Stolz, J.G.M. Kuerten, M. Nordlund, A.K. Kuczaj, B.J. Geurts, Fully-developed conjugate heat transfer in porous media with uniform heating, Int. J. Heat Fluid Flow. 38 (2012) 94–106.
[30] J. Ross-Jones, M. Gaedtke, S. Sonnick, M. Rädle, H. Nirschl, M.J. Krause, Conjugate heat transfer through nano scale porous media to optimize vacuum insulation panels with lattice Boltzmann methods, Comput. Math. with Appl. 77 (2019) 209–221.
[31] A.G. Fedorov, R. Viskanta, Three-dimensional conjugate heat transfer in the microchannel heat sink for electronic packaging, Int. J. Heat Mass Transf. 43 (2000) 399–415.
[32] M.O.R. Siddiqui, D. Sun, Finite element analysis of thermal conductivity and thermal resistance behaviour of woven fabric, Comput. Mater. Sci. 75 (2013) 45–51.
[33] F. Semeraro, J.C. Ferguson, M. Acin, F. Panerai, N.N. Mansour, Anisotropic analysis of fibrous and woven materials part 2: Computation of effective conductivity, Comput. Mater. Sci. 186 (2021) 109956.
[34] W. Owens, D. Merkel, F. Sansoz, D. Fletcher, Fracture Behavior of Woven Silicon Carbide Fibers Exposed to High-Temperature Nitrogen and Oxygen Plasmas, J. Am. Ceram. Soc 98 (2015) 4003–4009.
[35] A.C. Young, W.G. Davids, D.J. Whitney, J.D. Clapp, A.J. Goupee, Structural testing and analysis of a braided, inflatable fabric torus structure, Acta Astronaut 139 (2017) 189–200.